An Adiabatic Foehn Mechanism

Florentin Damiens [a] Francois Lott[a]* Christophe Millet [b] and Riwal Plougonven [c]

[a] *LMD Ecole Normale Supérieure, 75231 Paris, France*
[b] *CEA DAM DIF, 91297 Arpajon, France*
[c] *LMD Ecole Polytechnique, 91128 Palaiseau, France*

*Correspondence to: Laboratoire de Météorologie Dynamique, Ecole Normale Supérieure, 24 rue Lhomond, 75231 Paris France.
E-mail: flott@lmd.ens.fr

Atmospheric mountain flows produced when the incoming wind is small near the surface and continuously increases with altitude are evaluated with models of increasing complexity. All models confirm that foehn can be produced by a mountain gravity wave critical level mechanism, where the critical level is located below the surface. This mechanism does not involve humidity, upper level wave breaking, upstream blocking, downward wave reflections or hydraulic control as often suggested by popular theories. The first model used is a theoretical model which combines linear gravity wave dynamics with a nonlinear boundary condition: in this model the wave breaking does not feedback onto the dynamics by construction. Partial linear waves reflection are also minimized by using smooth profiles of the incident wind and a uniform stratification $N^2 = $ cte, and can even be suppressed when the incident wind shear is also constant, $U_z = $ cst. The second model is a numerical mesoscale model (Weather Research and Forecast), and we show that it predicts mountain wave fields that can be reproduced by the theoretical model, provided that we specify an adequate boundary layer depth in the theoretical model.

Received . . .

1. Introduction

Foehn flows are characterized by downslope winds that are warm, dry and strong and that generally occur on the lee side of mountains (Richner and Hachler 2013). For more than a century they have been studied worldwide (see for three different mountain ranges Brinkmann (1974); McGowan *et al.* (2002); Drobinski and Coauthors (2007)), because they have strong economical impacts, for instance through increase in fire danger (Takane and Kusaka 2011; Sharples *et al.* 2010; Cannon *et al.* 2017)), pollution (Seibert *et al.* 2000) or weather hazards. They can also actively contribute to the climate change through their local impacts on sea ice melting (Elvidge *et al.* 2015).

One long-standing question about foehn concerns the origin of the warming of the air masses, and it is generally admitted that there are two dominant mechanisms that can explain it (Richner and Hachler 2013). The first mechanism is along the line of meteorological textbooks (Seibert 2005) when the example of the foehn is used to illustrate the significance of moist processes by using thermodynamical diagrams. In this "diabatic" theory, the warming of the air masses results from the forced condensation that occurs upstream of the ridge, the large temperature and dry air result from the flow descent on the lee side. As observational evidence suggests that warming has a more adiabatic cause (Seibert 1990), a second mechanism, named "isentropic drawdown" is often proposed. In this mechanism, the foehn air comes from warmer and dryer altitudes upwind of the mountain because there is low level flow blocking. These two types of foehn, one diabatic with strong upstream ascent and one adiabatic with upstream flow blocking are sometimes referred to as Swiss and Austrian foehn respectively (Wursch and Sprenger 2015). With the progress of Lagrangian analysis, the relative amplitude of these two mechanisms is now better established (Smith *et al.* 2003; Miltenberger *et al.* 2016) and it seems that the adiabatic mechanism is often more efficient that the diabatic one. The Lagrangian analyses also reveal that other irreversible processes can play a role, like the vertical mixing occurring when the air passes the mountain summit, and the radiative impact of the upstream clouds (Elvidge and Renfrew 2016).

The fact that dynamics play such a central role in the foehn motivates the present paper. Actually, behind the apparently simple idea that upstream blocking elevates the air parcels before they abruptly descent on the lee side are hidden quite subtle nonlinear processes. These processes are controlled by the non dimensional mountain height, $H_N = \frac{HN}{U_\infty}$, where H is the maximum mountain height, N the buoyancy frequency and U_∞ a scale for the incident wind. When H_N is large, the vertical wavelength of the mountain waves U_∞/N is

small compared to the mountain height H, the mountain waves break near above the mountain top, and the resulting nonlinear dynamics produce strong downslope winds and foehn (see the review by Durran (1990) and recent simulations in Smith and Skyllingstad (2011)). The mixing produced by the breaking waves can induce a well mixed stagnant layer, which allows to establish a correspondence with the fully nonlinear hydraulic jump theory (Baines (1998); Smith (1985)). The presence of the stagnant layer also permits to argue that nonlinear reflections at the self-induced critical level present in the mixed layer can reflect downward the waves and amplify the response (Laprise and Peltier 1989; Smith and Skyllingstad 2011). Also, for large H_N, part of the low level flow is blocked upstream making upstream blocking concomitant to the onset of foehn. All these efforts to interpret dynamically the onset of foehn in terms of breaking waves or blocking, hide the simple fact that some foehn can be produced by Long (1953)'s model for hydrostatic linear waves forced by a nonlinear boundary condition (Lilly and Klemp 1979; Muraki 2011). Interestingly, using such a model, Lilly and Klemp (1979) predict that the wave response is enhanced for mountains with a small windward and large leeward slopes, which is a form of "isentropic drawdown" mechanism produced by blocking, if we assume that the blocked air can be represented dynamically by a gentle windward slope. Nevertheless, the results using Long (1953)'s type models are not much used to interpret foehn, essentially because when they produce foehn, they also predict intense wave breaking aloft which undermines all the linear interpretations of what occur downstream of the breaking zone (e.g which includes the foehn zone). As we shall see, low level wind shears can mitigate this upper level wave breaking because the mountain waves become less and less unstable with altitude when the wind increases.

Concerned with the recurrent problem in mountain meteorology theory that the near surface winds are ill defined (Vergeiner (1971); Lott (2007)) and can become very small, Lott (2016) (hereinafter L16) adapts the model of Long (1953) to incident shear flow that are null in $z = 0$. L16 shows that this induces a critical level dynamics near below the surface that produces downslope windstorm and foehn without upper level wave breaking. L16 also shows that downslope winds and foehn are favored when the surface flow is stable, i.e. when the surface Richardson number $J = N^2/U_z^2$ is large compared to its critical value, $J = 0.25$. As the model is linear, it also suggests that there is no need to interpret the onset of foehn in terms of upstream blocking, nonlinear internal wave reflections, or using hydraulic theory, which are all the ingredients that are often mentioned to explain adiabatic foehn.

The results in L16 have several limitations. The first is that the model in L16 is only adapted to situations when the shear layer depth, d, is much larger than the maximum mountain height, H, i.e as long as the near critical level solutions in Booker and Bretherton (1967) can be used to treat the critical level. The second is that L16 does not explain why the results found are so sensitive to J. The third is that it does not exclude the possibility that reflections can play a role on foehn, because linear reflections can be present. The fourth is that the inflow equations used in Long (1953) are only rigorously valid when the incident flow is uniform. The last is the representation of boundary layer absorptive effects: L16 uses Raighleigh drag and Newtownian cooling with a free slip boundary condition. Some earlier studies have explored more realistic boundary conditions, e.g. for turbulent flow over hills (Hunt *et al.* 1988a,b), or with viscous solutions Lott (2007). In L16, these simplifications are made to ease the numerical treatment of the problem. They are in part justified by the fact that in the atmosphere the low level wind shears are often due to horizontal gradients in temperature, they do not solely result from boundary layer dynamics: they can extend well above it, and there the inviscid dynamics can be applied.

The purpose of the present paper is to fill these gaps by extending the L16's theory to taller mountains, and by validating it against fully nonlinear simulations. For this purpose, section 2 reformulates the results in L16 for a mountain of arbitrary height (not only for $H << d$) but still for small dissipation (when the linear drags correspond to a boundary layer depth $z_b << d$). Section 3 exposes the dry foehn mechanism proposed and shows that it is entirely related to the near-surface critical level dynamics. Section 4 presents fully nonlinear simulations done with WRF and explains how the value of z_b is chosen to enable a comparison of the theory with the numerical simulations. Section 5 characterizes systematically the results in terms of foehn intensity, downslope winds amplitude, and gravity wave stress. To check if the results remain robust beyond our simplified treatment of the boundary layer, it also presents tests where (i) the incident wind is not null at the surface and (ii) where a conventional atmospheric boundary layer scheme is used. Section 6 concludes and discusses further the relations with observations.

2. Theoretical model

To analyze the mountain waves produced by a stably stratified shear flow when the incident wind is null at $z = 0$, L16 considers the background flow profiles

$$U(z) = U_\infty \tanh(z/d), N^2(z) = \text{const}, \tag{1}$$

incident on a 2-dimensional mountain, the height of which follows the Witch of Agnesi profile

$$h(x) = \frac{H}{1 + \frac{x^2}{2L^2}}. \tag{2}$$

In (1), $U(z)$ is the background horizontal wind, $N(z)$ the Brunt Vaisala frequency, z the altitude, d is the vertical scale of the shear and U_∞ the incident wind maximum amplitude. In (2) H is the maximum mountain height, L its characteristic horizontal length, and x the horizontal coordinate. When scaling time by N^{-1} and distances by U_∞/N the 2-dimensional non-rotating linear dynamics can be expressed in term of a non dimensional vertical velocity, $\overline{w}(\overline{x}, \overline{z})$ of the form,

$$\overline{w}(\overline{x}, \overline{z}) = \int_{-\infty}^{+\infty} f(\overline{k}) \hat{w}_c(\overline{k}, \overline{z}) e^{i\overline{k}\overline{x}} d\overline{k}, \tag{3}$$

where overbars denote dimensionless variables, and $\hat{w}_c(k, z)$ is a canonical monochromatic solution of "unit" amplitude in the far field which satisfies the dissipative Taylor Goldstein equation,

$$\frac{d^2 \hat{w}_c}{d\overline{z}^2} + \left[\frac{1}{\left(\overline{U} - i\frac{\overline{z}_k}{\sqrt{J}}\right)^2} - \frac{\overline{U}_{\overline{z}\overline{z}}}{\overline{U} - i\frac{\overline{z}_k}{\sqrt{J}}} - \overline{k}^2 \right] \hat{w}_c = 0. \tag{4}$$

88 In (3) the amplitude term $f(\overline{k})$ is obtained by numerical inversion of the non-linear free-slip boundary condition:

$$\overline{w}(\overline{x}, \overline{h}(x)) = \left(\overline{U}(\overline{h}) + \overline{u}(\overline{x}, \overline{h}(\overline{x})) \right) \partial_{\overline{x}} \overline{h}(x), \tag{5}$$

89 where $\overline{u}(\overline{x}, \overline{z})$ is the horizonatl wind disturbance. In (4)-(5)

$$\overline{U}(\overline{z}) = \tanh\left(\frac{\overline{z}}{\sqrt{J}} \right), \text{ and } \overline{h}(\overline{x}) = \frac{H_N}{1 + \overline{x}^2/2F_r^2} \tag{6}$$

90 where

$$J = \frac{N^2 d^2}{U_\infty^2}, \; H_N = \frac{HN}{U_\infty}, \text{ and } F_r = \frac{LN}{U_\infty} \tag{7}$$

91 are the surface and minimum Richardson number, a non-dimensional mountain height, and a Froude number respectively. Still in (4)
92 the dissipative vertical scale for each harmonics,

$$\overline{z}_k = \frac{\overline{z}_b}{2} \left(\frac{1}{F_r \overline{k}} + F_r \overline{k} \right). \tag{8}$$

93 has been expressed in terms of a global scale $\overline{z}_b$, with the first term in parenthesis resulting from Rayleigh drag and Newtonian
94 cooling of coefficient $\overline{z}_b/F_r * \sqrt{J}/2$ and the second term from a viscous dissipation which acts in the x-direction only of coefficient
95 $\overline{z}_b F_r/\sqrt{J}/2$ (see also the right hand sides of Eqs.4 in L16). They are introduced to regularize the critical level dynamics for all the
96 harmonics, i.e. the longer and the shorter ones respectively. Note that $\overline{z}_k$ is written differently than in L16 to make clear that when the
97 formula is applied to the dominant wavenumber Fr^{-1}, $\overline{z}_k$ in (8) compares to the dissipative scale $\overline{z}_b{}^*$.

98   To construct $\hat{w}_c$, L16 uses for each k an exact solution of the inviscid version of (4), $\hat{w}_{\text{inv}}(\overline{k}, \overline{z})$, which is based on hypergeometric
99 functions (see Lott *et al.* (1992) and (34) in L16), and which asymptotic behaviors are

$$\hat{w}_{\text{inv}}(\overline{k}, \overline{z} >> 1) \approx e^{-\overline{m}\,\overline{z}/\sqrt{J}}, \tag{9}$$

100

$$\hat{w}_{\text{inv}}(\overline{k}, \overline{z} << 1) \approx a_1(\overline{k})\overline{z}^{1/2-i\mu} + a_2(\overline{k})\overline{z}^{1/2+i\mu} \tag{10}$$

101 where,

$$\overline{m} = \sqrt{J}\sqrt{|\overline{k}^2 - 1|}, \; \mu = \sqrt{|J - \frac{1}{4}|}, \tag{11}$$

102 and where $a_1(\overline{k})$ and $a_2(\overline{k})$ have analytical forms once the "unit" amplitude condition (9) is satisfied. Also, when $\overline{k}^2 < 1$, $\overline{m}$ is changed
103 in $-i\text{sign}(\overline{k})\overline{m}$, where the sign is to ensure upward group speed. Near the surface, L16 also uses the asymptotic solution of the damped
104 Taylor-Goldstein Equation (4) valid when $\overline{z} << 1$:

$$\hat{w}_{\text{srf}}(\overline{k}, \overline{z}) = a_1(\overline{k})(\overline{z} - \overline{z}_k)^{1/2-i\mu} + a_2(\overline{k})(\overline{z} - \overline{z}_k)^{1/2+i\mu}, \tag{12}$$

105 where a_1 and a_2 are the same as in (10) to ensure matching. To establish how these aproximate solutions can be combined to provide a
106 uniformly valid approximation of $\hat{w}_c(\overline{k}, \overline{z})$, Fig. 1 shows $\hat{w}_{\text{inv}}(\overline{k}, \overline{z})$ (thin solid), its approximation near $z = 0$ ((10), thick dashed) and
107 $\hat{w}_{\text{srf}}(\overline{k}, \overline{z})$ (thick dashed and dots). For the three values of J selected, $J = 0.5, 2, 4$, we see that below around $z \approx J/4$ the inviscid exact
108 solution $\hat{w}_{\text{inv}}$ and its inviscid approximation on the right of (10) almost coincide whereas above this altitude the asymptotic damped
109 approximation ($\hat{w}_{\text{srf}}$ in (12)) and the asymptotic inviscid solutions (10) are very close. This suggests that we can take the altitude $J/4$
110 to make a transition between the exact inviscid solution and the asymptotic damped solution. In the following, this transition is made
111 by patching these two functions using $tanh$ tapers centered at $\overline{z} = J/4$ and of depth $\Delta \overline{z} = J/5$, i.e. by writting,

$$\hat{w}_c(\overline{k}, \overline{z}) = \frac{\left(1 + \tanh\left(\frac{5\overline{z}}{J} - \frac{5}{4} \right) \right)}{2} \hat{w}_{\text{inv}}(\overline{k}, \overline{z}) + \frac{\left(1 - \tanh\left(\frac{5\overline{z}}{J} - \frac{5}{4} \right) \right)}{2} \hat{w}_{\text{srf}}(\overline{k}, \overline{z}). \tag{13}$$

112 The thick gray curves in Figs. 1a, b, c show these new approximations, and illustrate how well they behave for all $\overline{z}$, permitting a
113 smooth passage from the damped solutions near the ground to the exact inviscid one in the far-field. Compared to L16, we use this
114 approximation in the inversion of (5),

$$\int_{-\infty}^{+\infty} f(\overline{k}) \left[\hat{w}_c(\overline{k}, \overline{h}) - \hat{u}_c(\overline{k}, \overline{h}) \frac{dh}{dx} \right] e^{i\overline{k}\overline{x}} d\overline{k} = U \frac{dh}{dx} \tag{14}$$

115 rather than using (12) to express $\hat{w}_c$ and $\hat{u}_c$ in the terms between brackets in (14). This formally permits to consider more elevated
116 ridges than in L16.

---

*For consistency, note also that the boundary layer depth $\overline{z}_B$ used in L16 is related to the one here by $\overline{z}_B = 5\overline{z}_b$.

3. A dry foehn mechanism

As the numerical results obtained with this new formulation of the model are consistent with those in L16 we will only emphasize on the descents of warm air that characterize foehn. In the following we take a domain of length 800 spanned by 1024 equally spaced points, the Froude number $F_r = 5$ and the boundary layer scale $\overline{z}_b = 0.05$. The three panels in the left column of Fig. 2 shows that when J increases the foehn effect increases, as expected from the results in L16, where the same behavior was discussed in terms of downslope windstorms. The reader is referred to this paper for more complete sensitivity tests to H_N and $\overline{z}_b$, but it is worthwhile to note here that when J passes 1 typically, an isentropic surface initially at the altitude of the ridge is not much displaced upward when it approaches the ridge but easily reaches the surface along the downslope side of the ridge (lowest dashed line in Fig. 2c). This "foehn" effect becomes extremely pronounced when $J = 4$ in Fig. 2e: almost all the air located between $H_N < \overline{z} < 2H_N$ upstream of the ridge descent below the mountain top $\overline{z} < H_N$ in the lee-side. Near the surface downstream, the theory predicts highly distorted isentropes and potential temperatures that are below the minimum value upstream: this is not realistic so they are not shown but this indicates where the dynamics may trigger breaking.

If the foehn effect proposed is purely related to the critical level dynamics, then it should be present in a theory that is even simpler than the one used to produce the panels on the left in Fig. 2. For this purpose we next derive the theory when the wind shear U_z and buoyancy frequency are both constant, in the hydrostatic approximation and when the boundary layer depth is identical for all harmonics $\overline{z}_k = \overline{z}_b$. As we will see in this "constant shear" case we can also formally eliminate the reflected waves, proving that they also play a minor role. To make clear that the dynamics in this case is only controlled by J and $\overline{z}_b$, the two parameters that control the critical level dynamics, we introduce a scaling suited to the constant wind shear configuration by taking for the horizontal and vertical scales those of the mountain. We also scale the horizontal velocity disturbance by the background velocity at the mountain top,

$$x = L\tilde{x}, z = H\tilde{z}, u = U_z H\tilde{u}, w = U_z H^2/L\tilde{w}, p = \rho_r U_z^2 H^2 \tilde{p}, \text{ and } b = U_z^2 H\tilde{b}. \tag{15}$$

In this new set-up and scaling, the Boussinesq dynamics writes

$$\tilde{z}\partial_{\tilde{x}}\tilde{u} + \tilde{w} = -\partial_{\tilde{x}}\tilde{p}, \ \partial_{\tilde{z}}\tilde{p} = \tilde{b}, \ \tilde{z}\partial_{\tilde{x}}\tilde{b} + J\tilde{w} = 0, \tag{16a}$$

$$\partial_{\tilde{x}}\tilde{u} + \partial_{\tilde{z}}\tilde{w} = 0, \ \tilde{w}(\tilde{z} = \tilde{h}) = \left(\tilde{h} + \tilde{u}\right)\frac{\partial \tilde{h}}{\partial \tilde{x}}, \tag{16b}$$

$$\tilde{h} = \frac{1}{1 + \tilde{x}^2/2}, \tag{16c}$$

it is only controlled by the Richardson number J. In this setup, we know that for each harmonics the vertical velocity is exactly,

$$\hat{w} = \tilde{z}^{1/2 + i\,\text{sign}(\tilde{k})\mu}, \tag{17}$$

where we have only retain the upward propagating solution (Booker and Bretherton 1967): there is no reflected wave by construction. We then incorporate a dissipative scale $\tilde{z}_k = \tilde{z}_b$ which we also take constant, a simplification that permits to define a canonical solution

$$\hat{w}_c(\overline{z}, \overline{k}) = \left(\tilde{z} - i\,\text{sign}(\tilde{k})\tilde{z}_b\right)^{1/2 + i\,\text{sign}(\tilde{k})\mu}. \tag{18}$$

We will next use this solution to evaluate the wave field in (3) and the boundary condition in (5). To ease comparison, the results will be shown using the dimensionless variables of the more complete theory,

$$\overline{x} = F_r\tilde{x}, \overline{z} = H_N\tilde{z}, \overline{u} = \frac{H_N}{\sqrt{J}}\tilde{u}, \overline{w} = \frac{H_N^2}{F_r\sqrt{J}}\tilde{w}. \tag{19}$$

The results from the simplified theory are shown in the right panels of Fig. 2, the resolutions being identical to those used to build the corresponding panels on the left. To have comparable results nevertheless we have taken a boundary layer scale that is smaller than that used in Section 2, $\overline{z}_b = 0.02$, a difference that is only related to our choice to take a constant boundary layer scale (if we adopt the formula (8) we need to return to the value $\overline{z}_b = 0.05$ to obtain the same results). With this scale, the simplified theory gives almost exactly the same results as the more complete one, at least at low level. As we emphasized previously, in this simplified theory, there is no reflected waves by construction, proving that the onset of foehn can be entirely due to the near surface critical level dynamics i.e. a mechanism summarized mathematically by (18), a mechanism that exclude pre-conditionning of a well mixed layer by upper level wave breaking, non-linear and now linear wave reflections.

Finally to understand further why the near-surface critical level dynamics makes the foehn so sensitive to J it is worthwhile to notice that for large J, the Booker and Bretherton (1967)'s solution (17) has an interpretation in terms of vertical wavenumber. To make this transparent we approximate it near the mountain top by writing $\overline{z} = H_N + \delta\overline{z}$, which yields

$$\overline{z}^{1/2 + i\mu} = \overline{z}^{1/2}e^{i\mu \ln \overline{z}} \approx \overline{z}^{1/2}H_N^{i\mu}e^{i\frac{\mu}{H_N}\delta\overline{z}}. \tag{20}$$

Near the mountain top, the disturbance has a characteristic wavenumber $\overline{m} \approx \mu/H_N$. Now, we know that mountain flow dynamics becomes nonlinear when the disturbance's vertical wavelength $\overline{m}^{-1}$ becomes smaller than the mountain height H_N. The argument often given is that in this case the linear theory predicts that vertical velocities change sign before the air parcels reach the mountain top. If we apply this condition here, we have that nonlinear effect become large when $H_N/\mu < H_N$, which approximately simplifies to the condition $J > 1$, which is the condition that favors foehn in the theory here and the downslope winds in L16.

Another point we make is that foehn is not associated with upper level wave breaking, i.e. that some form of wave breaking can occur below the mountain top without occurring aloft. To illustrate this qualitatively we next use the same line of arguments as before.

162 We compare the wave vertical wavelength $\overline{m}_B$ and the vertical displacement $\overline{\eta}_B$ produced by the wave around a "breaking" altitude
163 H_B, yet to be found, and by writing $\overline{z} = H_B + \delta\overline{z}$. This yields

$$\overline{m}_b \approx \mu/H_B \text{ and } \overline{\eta}_B \approx H_B^{-1/2+i\mu} H_N^{3/2-i\mu}. \tag{21}$$

164 respectively. Qualitatively, breaking occurs when $|\overline{\eta}_B| \geq \overline{m}_B^{-1}$, which gives,

$$H_B \leq \mu^{2/3} H_N. \tag{22}$$

165 Wave breaking is confined to the lowest layers, and inhibited above the mountain summit H_N at least when $\mu < 1$. This is the basic
166 reason due to which the foehn mechanism described here is not associated with upper level wave breaking. Of course this effect simply
167 translates the fact that in presence of shear, the vertical wavelength increases with altitude.
168 The result in (22) also illustrates that the depth of the layer over which breaking occurs increases with J. To a certain extent this
169 suggests that the dissipative layer depth should increase with J. As we will see next this is in fact the case when we compare to fully
170 nonlinear simulations.

4. Verification with fully nonlinear model

172 To extend the above results beyond the inflow-linear and Boussinesq approximations, we next use the WRF model in the 2D mountain
173 flow configuration available on line[†](Skamarock *et al.* 2008). It is configured here for a 100km long and 12km height domain gridded
174 by 1000×1000 points yielding resolutions of 100m and 12m in the horizontal and vertical directions respectively. At the lateral bounds
175 the domain is open and below the model top a 6km deep absorbing layer prevents the gravity waves to be reflected downward. These
176 quite high resolutions are to ensure that the near surface critical level dynamics is well represented. They require a time step $\Delta t = 0.5$s.
177 Note also that all the results from WRF shown next have been verified against simulations where the horizontal and vertical gridspacing
178 are divided by two. As the WRF model is fully compressible, it is mandatory to recall that in it the stratification is represented by a
179 Brunt Vaisala frequency given by $N^2 = \frac{g}{\theta_0}\frac{d\theta_0}{dz}$, where θ_0 is a background potential temperature. To ensure that it is constant and to
180 minimize the vertical variations of the background fields that could result in partial reflections, we consider an isothermal atmosphere
181 $T_r = 290$K, yielding $N^2 = \frac{\kappa g^2}{R T_r} = 3.10^{-4}\text{s}^{-2}$, where κ, R, and g have their conventional dry air and earth-values. We will then impose
182 the background wind (1) and always take $U_\infty = 10$m/s, the minimum Richardson number will then be changed by varying the shear
183 layer depth d. Also, the mountain height will be given by (2) with $L = 2.8$km to ensure $F_r = 5$.
184 Finally, in all the WRF simulations presented the dissipative coefficients are set to 0 and the surface boundary condition is free slip.
185 This does not mean that the simulations are inviscid, because irreversible and diabatic processes will necessarily occur if the model
186 confirms the onset of convective overturnings like those found in the theoretical model in the previous section. All the experiments
187 presented in the next section prove that the WRF dynamical core is stable and dissipative enough to handle these irreversible processes.
188 When we return to the theory, it is a priori difficult to say how these irreversible processes can be translated in the theorety. Nevertheless,
189 as the theory has a free parameter to represent dissipations, the boundary layer scale $\overline{z}_b$, we can vary it and try to identify a value
190 for which there is a match between the nonlinear simulations and the theory. To sort out this issue we have undertaken a systematic
191 comparison between the WRF model and the theoretical one, varying the boundary layer depth in the latter. We found a good agreement
192 when we take a boundary layer depth varying like

$$\overline{z}_b/\sqrt{J} = 0.05. \tag{23}$$

193 The 0.05 factor is purely empirical and little sensitive to the resolution in both models, but the $\sqrt{J}$ term suggests that between the
194 simulations and the theory, the penetration of the boundary layer depth into the shear layer needs to be the same.

4.1. Fixed mountain height

196 To confirm that theory can match the fully nonlinear simulation, we present experiments with a fixed mountain height $H = 250$m,
197 ($H_N = 0.5$), and vary the minimum Richardson number between $J = 0.5$ and $J = 5$. Figure (3) shows the horizontal wind disturbances
198 from the linear model (left) and the WRF model (right) for 3 different Richardson numbers ($J = 0.5, 2$, and 4). In each figure the contour
199 interval is proportional to the background wind amplitude at the top of the Hill ($\approx H_N/\sqrt{J}$), a value representative of the disturbance
200 amplitude needed to satisfy the lower boundary condition. The first striking result is that the left hand and right hand panels share
201 strong similarities: the wave amplitude and phase line tilts with altitude are comparable. Also, when J increases, the phase line tilts
202 with altitude become more and more vertical above the ridge, which means that the characteristic horizontal scale of the wave field
203 decreases when J increases: this behavior is consistently reproduced by the theory and by the WRF model. In all panels, we also note
204 that the horizontal wind disturbances are substantially larger on the downstream side ($\overline{x} > 0$). This upstream/downstream difference
205 becomes very pronounced near the ground, contrasting the two flanks of the mountain. It is this difference in horizontal winds that
206 explains why low level shears can produce intense downslope winds (L16), and we see here that it is also present in the simulations.
207 Returning to the foehn effect, Fig. 4 shows the isentropic surfaces corresponding to the experiments shown in Fig. 3. Again, the
208 results between the theory and WRF are quite consistent, some qualitative discrepancies emerge downstream where the simulations
209 start to predict potential temperature jumps. These figures also illustrate another feature: the theoretical results shown in Fig. 2 and
210 in Fig. 4 differ by the value of $\overline{z}_b$, which increases with J for the comparison with WRF (see eq. 23). Comparison of figures 2 and 4
211 shows that the increase of $\overline{z}_b$ limits the onset of foehn.

[†]www2.mmm.ucar.edu/wrf/users/downloads.html

212   *4.2.   Fixed penetration of the mountain into the shear*

213   As said before, to match the WRF simulations, we had to keep constant in the theoretical model, the ratio between the shear layer depth
214    $\sqrt{J}$ and the boundary layer scale $\overline{z}_b$. This limits the amplitude of foehn in the theoretical model, but does not make it disappear. To
215   make the Foehn effect more evident in the simulations, we next keep the "penetration" of the mountain into the shear constant between
216   the experiments by keeping $H_N/\sqrt{J}$ constant. In this case, at the top of the hill, the incident wind is the same in all the experiments,
217   and to a certain extent, it is only the stratification that is changed. Note also that in these experiments the ratio between the boundary
218   layer depth and the mountain height $\overline{z}_b/H_N$ is also constant, which allows cleaner comparisons of results since z_b now changes with
219    $\sqrt{J}$.

220   The results are shown in Fig. 5 for ($J = 0.5$, $H_N = 0.25$) and ($J = 4$, $H_N = 0.71$), the corresponding plots for ($J = 2$, $H_N = 0.5$)
221   being already in Figs 4c–d. Again, a good match between the theory and WRF is found, which is important since we are now using
222   non-dimensional mountain height that are near 1. In both the theoretical model and in WRF, the foehn downstream is now slightly more
223   substantial when $J = 4$ than when $J = 0.5$, but the difference are more in terms of horizontal distance over which the air descends on
224   the lee-side. In the simulation with $J = 4$ the isentrope which is at the altitude of the mountain summit upstream rapidly descends below
225   half the mountain top downstream, before returning to its upstream altitude after the passage through an hydraulic jump. Importantly
226   both this behavior and the location of the jump are well predicted by the theory. When $J = 0.5$ the descent of air in WRF is less abrupt,
227   in agreement with theory but the total descent is still about half the mountain height. Another point is worth noticing. In Figs. 5a-d,
228   but this is also true in all the other Figures, there is very little uplift of the air parcels in front of the ridge, the most spectacular vertical
229   displacements occur after the passage of the summit. This small uplift could suggest that diabatic effects should not much affect the
230   results, at least when the atmosphere is not close to water vapor saturation.

231   In this paper we try to make the point that upper level wave breaking is not needed for foehn to occur. The basic argument is that the
232   theory is linear, yet shows a very good agreement with the fully non linear simulations. Nonetheless, we can go one step further and
233   diagnose if upper level wave breaking actually occurs in WRF and in the theory. The answer is simply that it does not,and to illustrate
234   this the Figs. 5e-f display the isentropic surfaces over a much larger domain than in Figs. 5c–d. In no place, except in the downstream
235   lee side, the isentropes become almost vertical. This is in contrast with what is found with the Long's model with uniform U (see Fig. 1f
236   in L16). In it, downslope winds and foehn always occur in conjunction with upper level wave breaking.

5.   More systematic comparisons and alternative configurations

238   *5.1.   Quantitative indices*

239   To provide quantitive measures of our results we have built global indices characterizing our problem and conducted 64 pairs (theory
240   versus WRF) of experiments, 32 corresponding to the constant height cases described in *4.1.* and 32 to the constant penetration of the
241   mountain into the shear cases described in *4.2.* For the first index, we follow L16 and measure downslope windstorm intensity by,

$$A = \underset{\substack{\overline{z} < H_N/2 \\ 0 < \overline{x} < 5F_r}}{Max} \left(\frac{\overline{u}(\overline{x}, \overline{z})}{U(H_N/\sqrt{J})} \right). \tag{24}$$

242   The index A indicates to which extent the wind in the flow along the foothills (defined as the region with $z < H_N/2$ and $0 < x < 5F_r$)
243   exceeds the background wind at the top of the hill ($U(H/d)$). In terms of foehn it is an important index because when the descent is
244   rapid there is less time for diabatic effects to mitigate the warming of the air masses. The results in Fig. 6a somehow reproduce those
245   in L16: the downslope wind intensity increases with stability J. However the increases are not as spectacular as in Lott (2016) where
246   A much more easily reaches values above 1, but this is consistent with the fact that z_b increases with J. This constraint is the price to
247   pay for our theory to be consistent with the simulations.

248   As our theory reproduces mountain waves quite well (see Fig 3), we have also evaluated the wave stress in $z = 2\sqrt{J}$ (that is well
249   above the maximum mountain height and the low level shear) and compare it to the linear hydrostatic wave drag produced by the
250   mountain in (6) in a uniform flow of intensity $U(H_N) = \frac{H_N}{\sqrt{J}}$:

$$F^z = -\frac{\int_{-\infty}^{\infty} \overline{u}\,\overline{w}\,d\overline{x}}{\frac{\pi}{4} \frac{H_N^3}{\sqrt{J}}}. \tag{25}$$

251   Again, the curves in Fig.6b show that the theory and the nonlinear simulations are in good agreement. Interestingly, when the
252   penetration of the mountain into the shear stays constant and J increases, the normalized wave stress F^z increases well beyond 1.
253   This behavior is reminiscent of the high drag states often found in non linear mountain flow theory (Bacmeister and Pierrehumbert
254   1988).

255   Finally, to characterize foehn, we identify the highest altitude from which are coming the isentropic surfaces that arrive along the
256   downstream foothill, and normalize by the mountain maximum altitude. In our non-dimensional formalism where the background
257   potential temperature varies as $\overline{z}$ exactly, this is conservatively given by,

$$F_{hn} = \underset{\substack{\overline{z} < H_N/2 \\ 0 < \overline{x} < 5F_r}}{Max} \left(\frac{\overline{\theta} + \overline{z}}{H_N} \right). \tag{26}$$

258   Interestingly, in our models this factor is always near 1. In other words the dynamics forces isentropic surfaces that are upstream at
259   the altitude of the ridge to descend along the foothills downstream. Hereagain simulations and theory compare well. In both, the foehn
260   intensity increases with J, but as for the downslope winds intensity, it is less pronounced than when z_b is kept small and constant in
261   the theory (not shown).

5.2. Alternative configurations

In the real atmosphere the low level shears have at least two causes: the thermal gradients due to the presence of fronts and the effect of the boundary layer. The first imposes shears that extend well above the boundary layer, the second forces the winds to vanish at the surface. There is no reason, except simplicity, to consider that the shears associated with these two processes have similar values. In this sense, we could say that our almost inviscid interpretation of the wave dynamics above the boundary layer is only adapted to the shears produced via thermal wind balance, Raighleigh friction and Newtownian cooling being an ad hoc parameterizations of the boundary layer absorptive properties, an absorption that becomes very efficient when the incident wind is null at $z = 0$. To show that our results have more generality than this apparently "ad-hoc" setup, we next propose three experiments. In the first two, we keep the same models and setup as in Figs. 5c and 5d but shift vertically the mountain height by $H_N/10$, e.g. by writing,

$$\overline{h}(\overline{x}) = \overline{h} = \frac{H_N}{1 + \overline{x}^2/2F_r^2} + \frac{H_N}{10}. \tag{27}$$

Doing so there is no need to rewrite the theory but, from a dynamical point of view there is a major change: the incident wind is no longer exactly null at the surface. The results in Figs. 7a and 7b show that in this case the theory and WRF simulations are still consistent and that the foehn effects are almost identical to those when when the incident wind is null at $z = 0$ in Figs. 5c and 5d respectively.

In the third experiment, we return to the exact setup of WRF used in Fig. 5d, but instead of the free slip boundary layer condition we adopt a planetary boundary layer scheme that has been extensively used in WRF. The chosen configuration activates the vertical diffusion described in Hong and Pan (1996) with the surface conditions evaluated using similarity theory. At the surface we impose a constant potential temperature, with value equal to the upstream temperature value at $z = 0$ and take a roughness length $z_0 = 10cm$. The results for the potential temperature and after a non-dimensional time $\overline{t} \approx 100$, are shown in Fig. 7c. Again the results in term of foehn compare well with those in Fig. 5d, and this despite the fact that now the low level winds and temperature adapt themselves to more conventional surface boundary conditions.

6. Discussion

The central result of this paper is the resemblance between Fig.5c and Fig.5d. It shows that isentropic "drawdown", a dry mechanism of foehn, where air parcels do not ascend significantly on the upstream side of mountains before descending abruptly on the lee side can be produced in a model without inflow nonlinear effects. The mechanism at work is related to the near surface critical level dynamics that occurs for mountain waves, the critical level being located just below the lower boundary. In this case, the inflow linear dynamics anticipate well where the wave breaks as is often the case in gravity wave theory. Not surprisingly, in the presence of low level wind shear, mountain wave breaking is favored in regions located below the mountain top rather than above.

In essence, the results obtained illustrate the significance of low level wind shears and stability on mountain flow dynamics, something often noticed in mountain meteorology, at least in the context of trapped lee waves (Reinecke and Durran 2009; Georgelin and Lott 2001). In this context it is interesting to note that there are many field experiments where upstream soundings show low level shears (Doyle *et al.* 2011; Sheridan *et al.* 2007), generally related to advancing fronts (Lothon *et al.* 2003), when the low level shear is associated with thermal wind balance. It is also worth noticing that there are cases where foehn is observed in the absence of upper level wave breaking Flamant *et al.* (2002). Other aspects of the theory also have reasonable behavior. According to Richner and Hachler (2013) a forecaster's rule says that foehn winds rarely descend more than 2000m below the mountain crest. In all figures when the foehn is strong (for instance when $J \geq 2$ in Figs. 4–5) we note a comparable behavior, the foehn never extend down to $z = 0$ in the lee side in these cases. Also, downstream where the isentropic surface become vertical, there is always near the surface a pool of relatively cold air. It is interesting that such a pool has often been viewed as an active part of the foehn dynamics (Lothon *et al.* 2003), we see here that it can be a consequence of it.

All these remarks are not to say that we want here to replace the existing theories of adiabatic foehn by a completely new one, the message is rather to complement them. Actually, our upstream low level shear can be viewed as a form of blocking, since it imposes slow incident low level flows. Also, upper level mountain wave breaking tend to decelerate the low level flow, again our background profiles with slow low level winds can be viewed as a result of this process. Finally, our results show that linear models forced by a nonlinear boundary condition potentially have some skill, which can turn out to be useful since simplified linear models are still sometimes used to predict mountain wave operationally at a cheap numerical cost (Vosper 2003; Sheridan *et al.* 2017). Finally, one may note that the equations solved in the numerical simulations and in the linear theory differ in their treatment of boundary layer dissipation. For consistency one may wish that the WRF model and the theory be adapted to use the same dissipative processes. Nevertheless, we explored in Section 5 the sensitivity of the results to the precise boundary condition at the surface (non-zero surface wind or including a boundary layer parameterization) and these tests suggested that the foehn effects are robust to such changes.

References

Bacmeister JT, Pierrehumbert RT. 1988. On high drag states of nonlinear stratified flow over an obstacle. *J. Atmos. Sci.* **45**: 63–80.

Baines PG. 1998. *Topographic effects in stratified flows*. Cambridge University Press.

Booker JR, Bretherton FP. 1967. The critical layer for internal gravity waves in a shear flow. *J. Fluid Mech.* **27**: 102–109, doi:http://dx.doi.org/10.1017/S0022112067000515.

Brinkmann WAR. 1974. Strong downslope winds at boulder, colorado. *Mon. Wea. Rev.* **102**: 592–602.

319 Cannon F, Carvalho LMV, Jones C, Hall T, Gomberg D, Dumas J, Jackson M. 2017. Wrf simulation of downslope wind events in coastal santa barbara county.
320   *Atmos. Res.* **191**: 57–73, doi:10.1016/j.atmosres.2017.03.010.

321 Doyle JD, Gabersek S, Jiang Q, Bernardet L, Brown JM, Dornbrack A, Filaus E, Grubisic V, Kirshbaum DJ, Knoth O, Koch S, Schmidli J, Stiperski I, Vosper
322   S, Zhong S. 2011. An intercomparison of t-rex mountain-wave simulations and implications for mesoscale predictability. *Mon. Wea. Rev.* **139**: 2811–2831,
323   doi:http://dx.doi.org/10.1175/MWR-D-10-05042.a.

324 Drobinski P, Coauthors. 2007. Foehn in the rhine valley during map: A review of its multiscale dynamics in complex valley geometry. *Quart. J. Roy. Meteor.*
325   *Soc.* **133**: 897916.

326 Durran DR. 1990. Mountain waves and downslope winds. *AMS Meteorological Monographs* **23**: 59–83.

327 Elvidge AD, Renfrew IA. 2016. The causes of foehn warming in the lee of mountains. *Bull. Amer. Meteor. Soc.* **97**(3): 455–466.

328 Elvidge AD, Renfrew IA, King JC, Orr A, Lachlan-Cope TA, Weeks M, Gray SL. 2015. Foehn jets over the larsen c ice shelf, antarctica. *Quarterly Journal of*
329   *the Royal Meteorological Society* **141**(688): 698–713.

330 Flamant C, Drobinski P, Nance L, Banta R, Darby L, Dusek J, Hardesty M, Pelon J, Richard E. 2002. Gap flow in an alpine valley during a shallow south fhn
331   event: Observations, numerical simulations and hydraulic analogue. *Quart. J. Roy. Meteor. Soc.* **128**(582): 1173–1210, doi:10.1256/003590002320373256.

332 Georgelin M, Lott F. 2001. On the transfer of momentum by trapped lee waves. case of the iop3 of pyrex. *J. Atmos. Sci.* **58**: 3563–3580.

333 Hong SY, Pan HL. 1996. Nonlocal boundary layer vertical diffusion in a medium-range forecast model. *Mon. Wea. Rev.* **124**: 2322–2339.

334 Hunt JCR, Leibovich S, Richards KJ. 1988a. Turbulent shear flows over low hills. *Quart. J. Roy. Meteor. Soc.* **114**: 1435–1470.

335 Hunt JCR, Richards KJ, Brighton PWM. 1988b. Stably stratified shear flow over low hills. *Quart. J. Roy. Meteor. Soc.* **114**: 859–886.

336 Laprise R, Peltier WR. 1989. On the structural characteristics of steady finite-amplitude mountain waves over bell-shaped topography. *J. Atmos. Sci.* **26**: 586–
337   595.

338 Lilly DK, Klemp JB. 1979. The effects of terrain shape on nonlinear hydrostatic mountain waves. *Journal of Fluid Mechanics* **95**(2): 241261, doi:
339   10.1017/S0022112079001452.

340 Long RR. 1953. Some aspects of the flow of stratified fluids; 1. a theoretical investigation. *Tellus* **5**: 42–58.

341 Lothon M, Druilhet A, Bnech B, Campistron B, Bernard S, Sad F. 2003. Experimental study of five fhn events during the mesoscale alpine programme:
342   From synoptic scale to turbulence. *Quarterly Journal of the Royal Meteorological Society* **129**(592): 2171–2193, doi:10.1256/qj.02.30, URL http:
343   //dx.doi.org/10.1256/qj.02.30.

344 Lott F. 2007. The reflection of a stationary gravity wave by a viscous boundary layer. *J. Atmos. Sci.* **139**: 3363–3371, doi:http://dx.doi.org/10.1175/JAS4020.1.

345 Lott F. 2016. A new theory for downslope windstorms and trapped lee waves. *J. Atmos. Sci.* **73**: 3585–3597, doi:doi:10.1175/JAS-D-15-0342.1.

346 Lott F, Kelder H, Teitelbaum H. 1992. A transition from kelvin-helmholtz instabilities to propagating wave instabilities. *Physics of Fluids A* **4**: 1990–1997,
347   doi:http://dx.doi.org/10.1063/1.858368.

348 McGowan HA, Sturman AP, ans P Zawar-Reza MK. 2002. Observations of foehn onset in the southern alps, new zealand. *Meteor. Atmos. Phys.* : 215–230.

349 Miltenberger AK, Reynolds S, Sprenger M. 2016. Revisiting the latent heating contribution to foehn warming: Lagrangian analysis of two foehn events over the
350   swiss alps. *Quarterly Journal of the Royal Meteorological Society* **142**(698): 2194–2204.

351 Muraki DJ. 2011. Large-amplitude topographic waves in 2d stratified flow. *J. Fluid Mech.* **681**: 172–192, doi:10.1017/jfm.2011.187.

352 Reinecke PA, Durran DR. 2009. Initial-condition sensitivities and the predictability of downslope winds. *J. Atmos. Sci.* **66**: 3401–3418, doi:http://dx.doi.org/10.
353   1175/2009JAS3023.1.

354 Richner H, Hachler P. 2013. Understanding and forecasting alpine foehn. *Mountain Weather and Forecasting* : 219–260doi:10.1007/978-94-007-4098-3_4.

355 Seibert MR, Feldman H, Neininger B, Baumle M, Trickl T. 2000. South foehn and ozone in the eastern alps - case study and climatological aspects. *Atmospheric*
356   *Environment* : 1379–1394.

357 Seibert P. 1990. South foehn studies since the alpex experiment. *Meteor. Atmos. Phys.* : 91–103.

358 Seibert P. 2005. Hanns thermodynamic foehn theory and its presentation in meteorological textbooks in the course of time. *From Beaufort to Bjerknes and*
359   *Beyond, Algorismus* **52**: 169–180.

360 Sharples JJ, Mills GA, McRae RHD, Weber RO. 2010. Foehn-like winds and elevated fire danger conditions is southeastern australia. *J. Appl. Meteor. Climatol.*
361   **49**: 1067–1095, doi:10.1175/2010JAMC2219.1.

362 Sheridan P, Vosper S, Brown P. 2017. Mountain waves in high resolution forecast models: Automated diagnostics of wave severity and impact on surface winds.
363   *Atmosphere* **8**(1): 24.

364 Sheridan PF, Horlacherxi V, Rooney GG, Hignett P, Mobbs SD, Vosper S. 2007. Influence of lee waves on the near surface flow downwind of the pennines.
365   *Quart. J. Roy. Meteor. Soc.* **133**: 1353–1369, doi:10.100a/2qj.110.

366 Skamarock WC, Klemp JB, Dudhia J, Gill DO, Barker DM, Duda MG, Huang XY, Wang W, Power JG. 2008. A description of the advanced research wrf
367   version 3. *NCAR Tech. Note* : 113ppdoi:doi:10.5065/D68S4MVH.

368 Smith CM, Skyllingstad ED. 2011. Effects of inversion height and surface heat flux on downslope windstorms. *Mon. Wea. Rev.* **139**: 3750–3764, doi:
369   http://dx.doi.org/10.1175/2011MWR3619.1.

370 Smith RB. 1985. On severe downslope winds. *J. Atmos. Sci.* **42**: 2597–2603, doi:http://dx.doi.org/10.1175/1520-0469(1985)042⟨2597:OSDW⟩2.0.CO;2.

371 Smith RB, Jiang Q, Fearon MJ, Tabary P, Dorninger M, Doyle JD, Benoit R. 2003. Orographic precipitation and air mass transformation: An alpine example.
372   *Quart. J. Roy. Meteor. Soc.* **129**: 433–454, doi:10.1256/qj.01.212.

373 Takane Y, Kusaka H. 2011. Formation mechanisms of the extreme high surface air temperature of 40.9c observed in the tokyo metropolitan area: Considerations
374   of dynamic foehn and foehnlike wind. *J. Appl. Meteor. Climatol.* **50**: 1827–1841, doi:DOI:10.1175/JAMC-D-10-05032.1.

375 Vergeiner I. 1971. An operational linear lee wave model for arbitrary basic flow and two-dimensional topography. *Quart. J. Roy. Meteor. Soc.* **97**(411): 30–60.

376 Vosper SB. 2003. Development and testing of a high resolution mountain-wave forecasting system. *Meteorological Applications* **10**(1): 75–86.

377 Wursch M, Sprenger M. 2015. Swiss and austrian foehn revisited: A lagragian based analysis. *Meteorologische Zeischrift* **24**: 225–242.
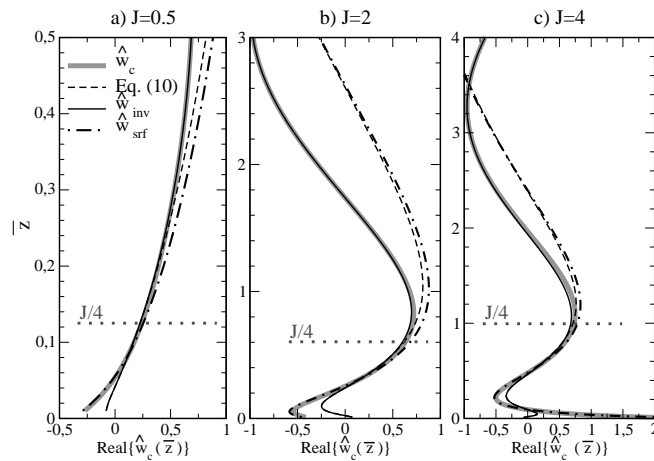
Figure 1. Vertical profiles of the solutions used to build the canonical solution: inviscid exact solution $\hat{w}_{inv}(\overline{k}, \overline{z})$ (black solid), approximation of $\hat{w}_{inv}(\overline{k}, \overline{z})$ near $\overline{z} = 0$ (right of (10), black dashed), damped approximation $\hat{w}_{surf}$ (12, black dashed and dot), and approximation of $\hat{w}_c(\overline{k}, \overline{z})$ (thick gray). In all panels, only the real part of the complex functions are shown, $\overline{k} = 0.1$ and $\overline{z}_b = 0.05$ for $J = 0.5, 2$, and 4 in a) b) and c) respectively.
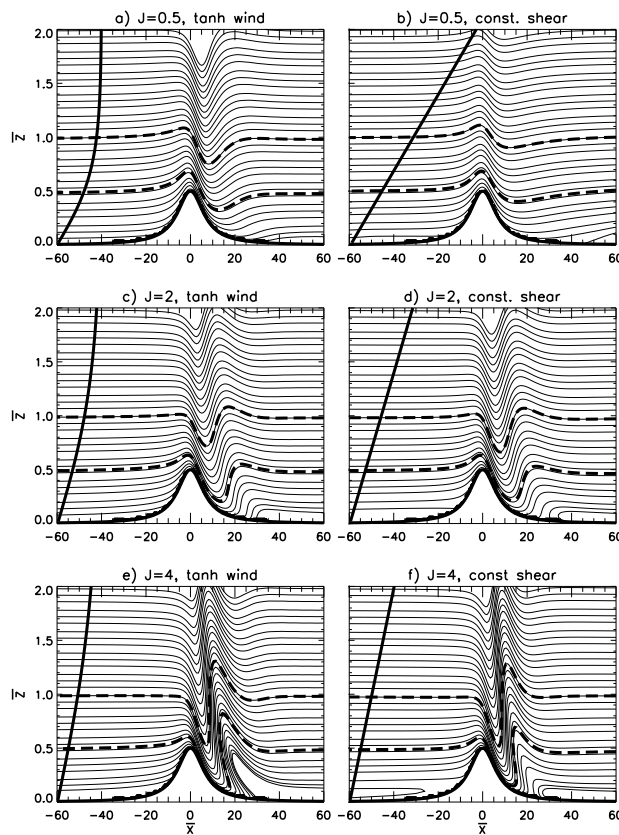
Figure 2. Isentropic surfaces predicted by the linear model when $H_N = 0.5$, $F_r = 5$ and for different value of J. Tanh incident wind and $\overline{z}_b = 0.05$: a) J=0.5, c) J=2, e) J=4. Constant shear and hydrostatic set-up in (16), $\overline{z}_b = 0.02$: b) J=0.5, d) J=2, e) J=4. In all panels the thick curve represent the incident wind U and the thick dashed curves the isentropes that initially are at the altitudes $\overline{z} = H_N$ and $\overline{z} = 2H_N$.
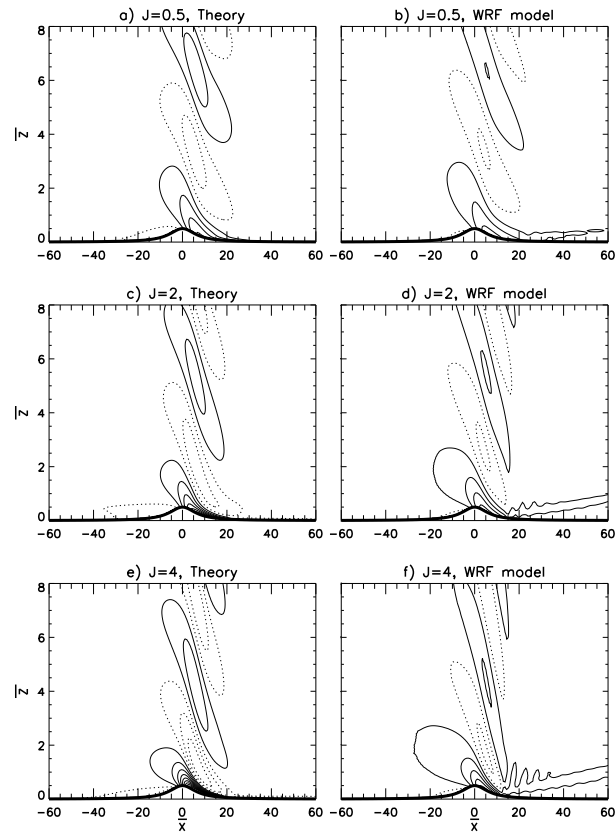
Figure 3. Non-dimensional Horizontal wind disturbances ($\overline{u}$) predicted by the theory (a, c, e) and WRF (b, d, f), for $J = 0.5$, 2, and 4, respectively. In all simulations $H_N = 0.5$ and in the linear model in (a), (c), and (e) the boundary layer scale varies as $\overline{z}_b = 0.05\sqrt{J}$. In each panel the contour interval is proportional to the background wind at the top of the hill, contours$= 0.2 * H_N / \sqrt{J}$.
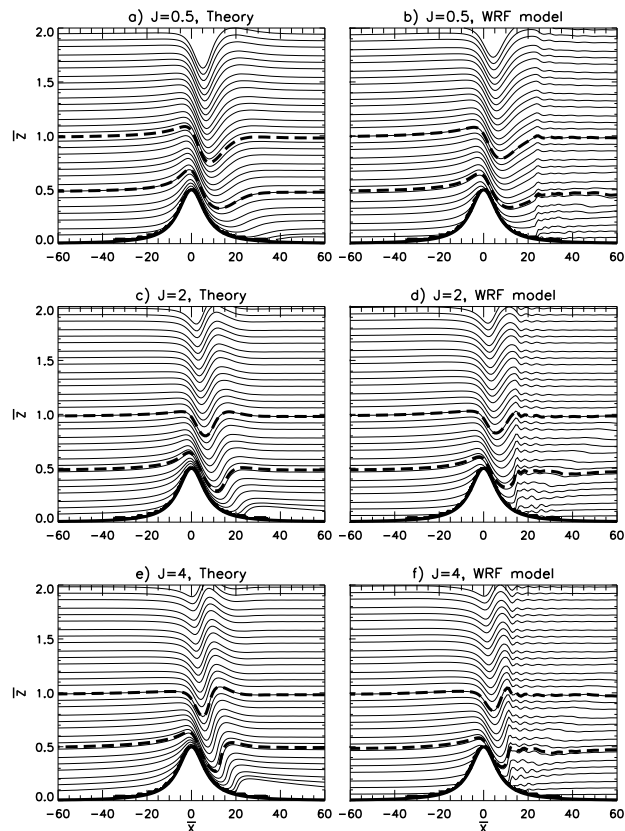

Figure 4. Isentropic surfaces predicted by the theory and WRF, same parameters as in Fig. 3
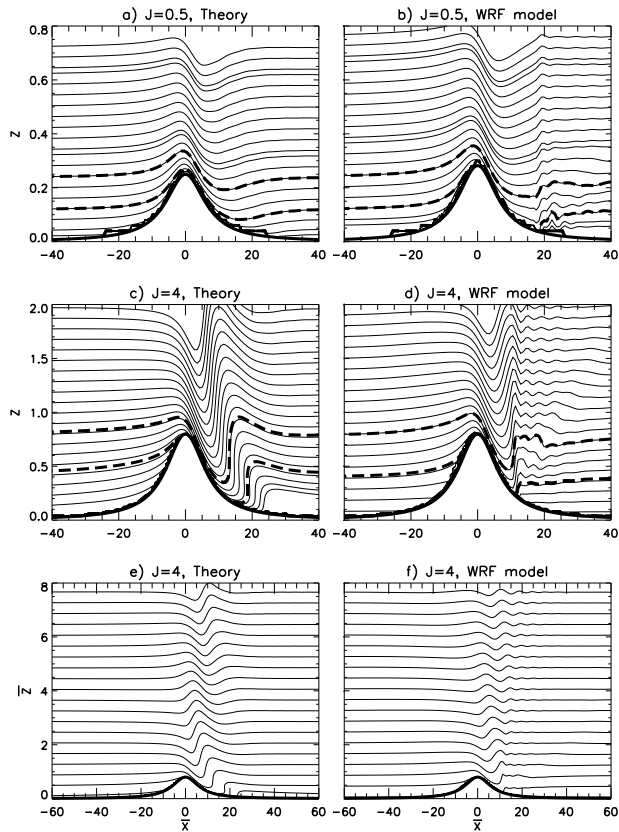
Figure 5. Same as Fig. 4 but leaving $H_N/\sqrt{J}$ =cte: a) and b) $J = 0.5$, $H_N = 0.25$; c) and d) $J = 4$, $H_N = 0.71$. e) and f) are enlarged views of c) and d).
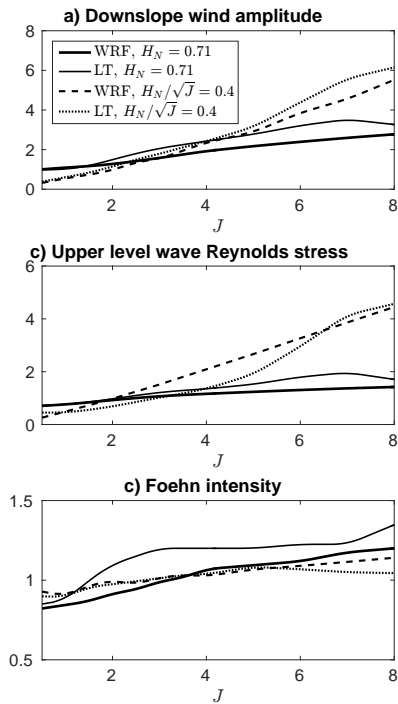

Figure 6. Global indices measuring a) the downslope wind amplitudes (24), b) the normalised wave stress (25), and c) the foehn intensity (26). The results are from 64 numerical experiments, 32 uses with WRF and 32 the "inflow linear" theory (LT). Half the simulations are done with constant height $H_N = 0.71$, the other half with constant penetration of the mountain into the shear $H_N/\sqrt{J} = 0.4$.
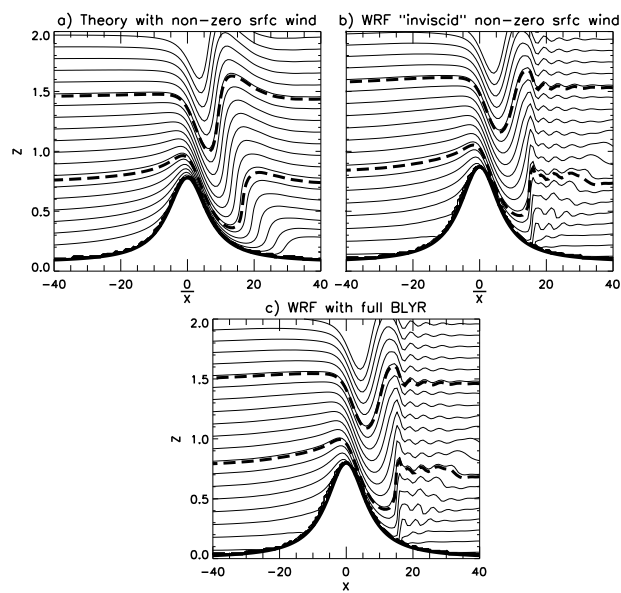
Figure 7. Sensitivity test: a) and b) are as Fig. 5c and 5d with the surface $\overline{h}$ shifted vertically by $H_N/10$. c) is as Fig. 5d but with a fully parameterized boundary layer.